


Phase-Modulated Cavity Magnon Polaritons as a Precise Magnetic Field Probe

Nicolò Crescini^{1,2,*}, Giovanni Carugno,^{1,3} and Giuseppe Ruoso²

¹*Dipartimento di Fisica e Astronomia, Via Marzolo 8, Padova 35131, Italy*

²*INFN-Laboratori Nazionali di Legnaro, Viale dell'Università 2, Legnaro (PD) 35020, Italy*

³*INFN - Sezione di Padova, Via Marzolo 8, Padova 35131, Italy*

 (Received 30 September 2020; revised 2 August 2021; accepted 2 September 2021; published 21 September 2021)

We describe and operate a spin-magnetometer based on the phase modulation of cavity magnon polaritons. In this scheme a rf magnetic field is detected through the sidebands it induces on a pump, and the experimental configuration allows for a negligible pump noise and a high-frequency readout. The demonstrator setup, based on a copper cavity coupled to an yttrium iron garnet sphere hybrid system, reached a sensitivity of $2.0 \text{ pT}/\sqrt{\text{Hz}}$ at 220 MHz, evading the pump noise and matching the theoretical predictions. An optimized setup can attain a rf magnetic field sensitivity of about $8 \text{ fT}/\sqrt{\text{Hz}}$ at room temperature. An orders of magnitude improvement is expected at lower temperatures, making this instrument one of the few magnetometers accessing the subfemtotesla limit.

DOI: [10.1103/PhysRevApplied.16.034036](https://doi.org/10.1103/PhysRevApplied.16.034036)

I. INTRODUCTION

The detection of ultralow magnetic fields is a long standing technological challenge. The most sensitive types of magnetic field detectors are essentially superconducting quantum interference devices (SQUIDs) [1–5] and spin-exchange relaxation-free (SERF) [6–8] magnetometers, which reach the $\text{fT}/\sqrt{\text{Hz}}$ sensitivity. Medical applications, such as nuclear magnetic resonance detection, is possibly the most studied utilization of such devices [9]. Remarkable results have been obtained with both SQUIDs [10–16] and SERF magnetometers [17–21]. In the last decades several magnetic field sensors have been proposed or demonstrated [22–33], making precision magnetometry an alive and dynamic field. SQUIDs are based on Josephson junctions and require cryogenic temperatures to be operated. Room-temperature devices are advantageous for cost and possible applications. SERF magnetometers do not need cryogenics, but require heavy shielding and their sensitivity is volume dependent.

This letter presents a magnetometer that embodies room-temperature operation, size-independent sensitivity, and rf working frequency. It is based on the phase modulation of a pump field exciting a cavity magnon polariton resonance. Measurements of extremely weak fields are possible by the detection of a sideband component induced on the input pump, allowing for the sensing of signals from a few megahertz to some gigahertz. Its expected limit sensitivity is competitive with present state-of-the-art magnetometers and could find application, for example,

in medical imaging, communication, and fundamental physics research [8,34–36].

The working principle of this device is based on the excitation of the Larmor transition in a magnetic material. By taking a ferrite or a paramagnet and biasing it with a static field \mathbf{B}_0 we obtain an electron spin resonance at frequency $\omega_L = \gamma B_0$, where $\gamma = (2\pi)28 \text{ GHz/T}$ is the electron gyromagnetic ratio. The presence of a weak magnetic field \mathbf{b}_1 , with frequency ω_b , has different effects. If \mathbf{b}_1 is perpendicular to \mathbf{B}_0 and on-resonance with ω_L , it will accumulate power into the Larmor transition, whose amount is proportional to \mathbf{b}_1 and can be used to measure it [37,38]. In the complementary case where the direction of \mathbf{b}_1 is parallel to the static field, the total field determining the Larmor transition is time modulated and will periodically change the frequency of the spin resonance. A microwave tone pumping the magnetic material at frequency ω_L will thus be phase modulated due to \mathbf{b}_1 with the result of producing sidebands at frequencies $\omega_L \pm n\omega_b$, with n an integer number. The detection of the sidebands will eventually give a measurement of the weak perturbing magnetic field [33]. The device we present in this letter originates by embedding the second scheme in a photon magnon hybrid system (PMHS).

II. DETECTION SCHEME

A PMHS consists of two coupled harmonic oscillators, e.g., the normal mode of a microwave cavity and the electron spin resonance of a magnetic material [39–41]. A typical realization of such a system is obtained by properly inserting in a copper microwave cavity a sphere of yttrium iron garnet (YIG), a ferrimagnetic insulator with

*nicolo.crescini@phd.unipd.it

high spin density and low losses [42–44]. Antennas coupled to the cavity are used for inserting and extracting power from the system. An external static magnetic field \mathbf{B}_0 is used to tune the Larmor frequency of electrons in YIG to the cavity mode frequency and couple the two systems. For ω_L close to the cavity frequency ω_0 , the cavity mode splits into two hybrid modes with frequencies ω_1 and ω_2 , where $g_{21} = \min(\omega_2 - \omega_1)/2$ is the coupling strength. If $g_{21} > \gamma_{1,2}$, the hybrid modes linewidth, the system is in the strong coupling regime. The resulting system can be described by quasiparticles called cavity magnon polaritons (CMPs), whose dispersion relation is an anticrossing curve [45–47].

Let us consider an oscillating field \mathbf{b}_1 parallel to the static one, and apply a monochromatic tone on one of the hybrid modes, like that at frequency ω_2 . As in the case of the simple system described before, the oscillating field will produce a frequency modulation of ω_2 , thus causing a phase modulation of the electromagnetic field stored in the PMHS, and sidebands are generated at frequencies $\omega_2 \pm n\omega_b$. However, since the PMHS has only two resonant modes, for $\omega_b > \gamma_2$, only the sideband satisfying the relation $\omega_2 \pm n\omega_b = \omega_1$ will be present and all others will be suppressed. By detecting the power at ω_1 , it will be possible to obtain a measurement of the perturbing field. For small fields, the only component with significant amplitude corresponds to $n = 1$ and this system is sensitive to fields whose frequency is $\omega_b = 2g_{21}$. With a PMHS the transduction coefficient between B_0 and the mode frequency is not given anymore by the gyromagnetic ratio but by a smaller coefficient $\alpha\gamma$. Such a coefficient, extracted from $\partial\omega_{1,2}/\partial B_0$, is practically γ for hybrid modes far away from the cavity resonance, while it goes to zero for a hybrid mode close to it. In the case of full hybridization, namely $\omega_2 - \omega_0 = \omega_0 - \omega_1 = g_{21}$, we have $\alpha = 1/2$.

A scheme of the spin-magnetometer principle is reported in Fig. 1(a). The monochromatic tone can be written as $A_0 \cos[\omega_2 t + \phi_b(t)]$, where $\phi_b(t)$ is an oscillating phase added by the field $|\mathbf{b}_1| = b_1 \sin(\omega_b t)$. The resulting phase modulated signal is

$$\xi(t) = A_0 e^{-i\omega_2 t} e^{-ix \sin(\omega_b t)}, \quad (1)$$

where x is the modulation index given by the maximum deviation divided by the working frequency

$$x = \pi \alpha Q_2 b_1 / B_0. \quad (2)$$

Here, $Q_2 = \omega_2 / \gamma_2$ is the quality factor of the hybrid resonance. For small values of x , Eq. (1) can be recast in terms

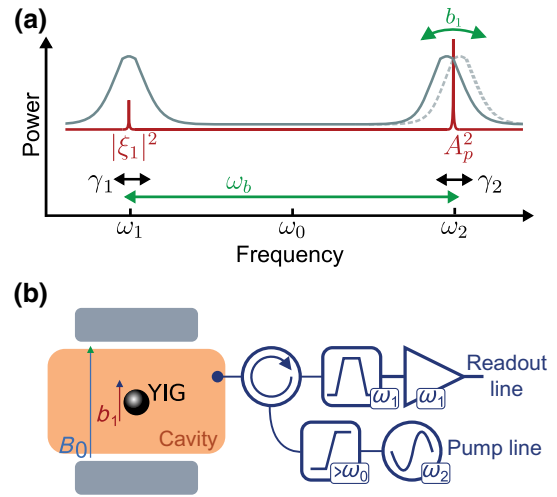


FIG. 1. (a) Scheme of the spin-magnetometer working principle. The gray line represents the transmission spectrum of the PMHS, the dark red line is the pump with the corresponding sideband, the magnetic field effect and its frequency are reported in green. (b) Electronics of an example device. The pump line is filtered with a waveguide with cutoff around ω_0 before exciting the ω_2 resonance. An antenna (full dot) is used to inject the tone and extract the sideband. The output power is filtered and amplified before the readout.

of the first kind Bessel functions $J_n(x)$ as

$$\begin{aligned} \xi(t) &= \sum_{n=0}^{+\infty} \xi_n(t) \\ &= A_0 e^{-i\omega_2 t} \sum_{n=0}^{+\infty} J_n(x) e^{-in\omega_b t} \\ &\simeq A_0 e^{-i\omega_2 t} \sum_{n=0}^{+\infty} \frac{x^n}{2^n n!} e^{-in\omega_b t}, \end{aligned} \quad (3)$$

where n is a positive integer. The amplitudes of carrier and lower-order sidebands are

$$|\xi_0| = A_0, \quad |\xi_1| = \frac{\pi \alpha A_0 Q_2 b_1}{2 B_0}, \quad |\xi_2| = \frac{1}{8} \left(\frac{\pi \alpha A_0 Q_2 b_1}{B_0} \right)^2. \quad (4)$$

The first-order sideband ξ_1 has the higher amplitude, and by comparing it with the backgrounds, it allows one to calculate the magnetometer's sensitivity to b_1 .

The scheme for a possible experimental setup is shown in Fig. 1(b). A signal generator provides the tone at ω_2 , filtered by a waveguide with cutoff frequency between ω_1 and ω_2 . The waveguide reduces the pump noise at frequency ω_1 by a factor k_1 that could be as large as 80 dB, depending on the separation between the cutoff and pump frequencies. The waveguide output is fed to the PMHS, namely a resonant cavity with YIG inside, in the total field

$\mathbf{B}_0 + \mathbf{b}_1$. The antenna has couplings $\beta_{1,2}$ to the two resonant modes, respectively. The power reflected from the cavity is bandpass filtered and amplified before the readout. The filtering removes the residual pump tone, avoiding saturation of the amplifier.

In an experimental setup we consider $Q_2 = Q_2^{(0)}/(1 + \beta_2) = Q_2^L$, the loaded quality factor of the CMP resonance. The output power at frequency $\omega_1 = \omega_2 - \omega_b$, normalized with the amplifier gain G_1 and filter transmittance c_1 , is given by

$$\begin{aligned} \frac{P_s(\omega_1)}{G_1 c_1} &= \frac{\beta_1}{1 + \beta_1} |\xi_1|^2 + k_1 \left(\frac{1 - \beta_1}{1 + \beta_1} \right)^2 A_p^2 |\text{RAM}(\omega_b)|^2 \delta\nu + k_B \left[\frac{4\beta_1}{(1 + \beta_1)^2} T + T_n \right] \delta\nu \\ &= A_p^2 \left[\frac{\beta_1}{1 + \beta_1} \frac{4\beta_2}{(1 + \beta_2)^2} \left| \frac{\pi\alpha Q_2^{(0)} b_1}{2(1 + \beta_2) B_0} \right|^2 + k_1 \left(\frac{1 - \beta_1}{1 + \beta_1} \right)^2 |\text{RAM}(\omega_b)|^2 \delta\nu \right] + k_B \left[\frac{4\beta_1 T}{(1 + \beta_1)^2} + T_n \right] \delta\nu. \end{aligned} \quad (5)$$

Here $\text{RAM}(\omega_b)$ is the relative residual amplitude modulation of the pump at ω_b . The absorbed pump power at ω_2 is $A_0^2 = 4\beta_2 A_p^2 / (1 + \beta_2)^2$, k_1 is the waveguide transmittance at ω_1 , k_B is the Boltzmann constant, T is the cavity temperature, T_n is the detection chain noise temperature, and $\delta\nu$ is the resolution bandwidth. Cables and circulators have been considered lossless. The first term in Eq. (5) is the searched-for signal, and consists essentially of the sideband power $|\xi_1|^2$. The following terms are the sources of noise, which are related to the pump and to the system noise temperature. The typical behavior of $\text{RAM}(\omega)$ shows large values at low frequencies with $1/f$ -like trend up to a few megahertz. All the terms are weighted with the appropriate combination of the antenna coupling constant to the first hybrid mode β_1 . At more than 10 MHz the noise of a commercial pump is flat with values $|\text{RAM}(\omega)|^2 \simeq -160$ dBc/Hz; the best oscillators reduce this limit down to -180 dBc/Hz [48]. This noise can then further reduced to a negligible level by using the waveguide filtering accounted by the term k_1 , obtaining a thermal-noise-limited device. In this limit we calculate the sensitivity σ_{b_1} of the apparatus, defined as the value of b_1 giving a $\text{SNR} = 1$ in unit time

$$\sigma_{b_1} = \frac{2\eta B_0}{\pi\alpha Q_2^L} \sqrt{\frac{k_B T_s}{A_p^2}}, \quad (6)$$

where the antennas coupling correction η and system noise temperature T_s are

$$\eta = \frac{(1 + \beta_2)}{2} \sqrt{\frac{1 + \beta_1}{\beta_2 \beta_1}}, \quad T_s = \frac{4\beta_1 T}{(1 + \beta_1)^2} + T_n. \quad (7)$$

With typical values $\beta_{1,2} \simeq 1$, $Q_2^L = 10^4$, $B_0 = 0.4$ T, $A_p^2 = 100$ mW, $T_s = 350$ K, and by working in the dispersive regime (i.e., with $\alpha \sim 1$) a sensitivity $\sigma_{b_1} \simeq 8$ fT/ $\sqrt{\text{Hz}}$ is expected already at room temperature.

Notably, the sensitivity reported in Eq. (6) is unrelated to any extensive property of the setup. This is expected in a scheme based on phase modulation rather than absorption [33,37], and paves the way to the miniaturization of the sensor without expecting a sensitivity loss. It needs to be considered that a strongly coupled PMHS often requires a large quantity of material, which might effectively limit the down scaling of the setup. However, this can be compensated by a more concentrated cavity field, which increases the single spin coupling and allows for using less magnetic material.

This magnetometer only works in a narrow frequency band corresponding to the linewidth γ_1 of the detection mode ω_1 . For a strongly coupled PMHS, this means detection of ac magnetic fields with frequency of order $2g_{21}$, which in the present case is about 200 MHz. Since ω_1 can be tuned via B_0 , the working frequency of the device can be changed, with the downside of reducing the sensitivity. Although a dedicated model has not yet been written, the reduction is expected to be $O(1)$ for a tuning of about 100 MHz [49], where the dispersive coupling might even increase the sensitivity as $\alpha \rightarrow 1$. We refer to this frequency range as the dynamical bandwidth of the magnetometer [49]. In general, the operational frequency of this class of magnetometers is limited from above by the largest strong coupling that can be reached, and from below by a combination of pump noise and filtering. While the former only depends on the hybrid system under consideration and can be of several gigahertz, the latter is mostly instrumental. To preserve the validity of Eq. (6), $\text{RAM}(\omega_b)$ must be reduced by k_1 to have $k_1 \text{RAM}(\omega_b) \lesssim k_B T_s$, which is increasingly difficult at lower ω_b due to the filter slope and to the higher pump noise. With present means, a lower limit for this frequency can be set around 10 MHz. Arbitrarily low frequencies can be reached at the price of a much lower sensitivity.

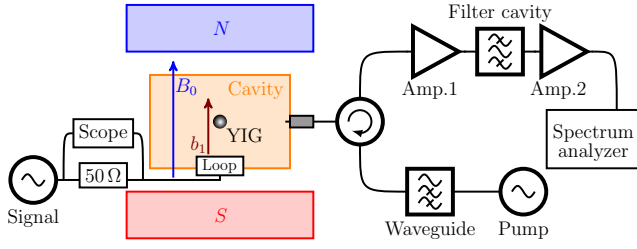


FIG. 2. Scheme of the magnetometer demonstrator. The calibration signal b_1 (dark red) is provided by a generator connected to a loop on the holed side of the cavity, and is monitored with an oscilloscope. The cavity (orange) houses a YIG sphere (black), which is biased with the static field B_0 supplied by an electromagnet represented with its north (N, blue) and south (S, red) poles. The rf cavity field is extracted by an antenna with variable coupling (gray), and passes through a circulator before being amplified by Amp.1 and Amp.2, while the filter cavity avoids the saturation of the second amplifier. The microwave pumping line delivers to the cavity a monochromatic tone filtered with a waveguide.

III. EXPERIMENTAL DEMONSTRATION

To demonstrate the operation of the magnetometer, we built the apparatus of Fig. 2. It features a microwave copper cavity 32.1 mm long, with a quasirectangular section of $14.8 \times 24.8 \text{ mm}^2$, as the shorter sides are rounded. A 2-mm diameter YIG sphere is placed at the center of the cavity, where the rf magnetic field of the chosen TM_{102} mode is maximum. The mode frequency is $\omega_0/2\pi \simeq 11.43 \text{ GHz}$, and the static field necessary to create the PMHS is $B_0 = \omega_0/\gamma \simeq 0.4 \text{ T}$, provided by an electromagnet with a bore of 10 cm diameter. The resulting hybrid modes resonate at $\omega_1 \simeq (2\pi)11.33 \text{ GHz}$ and $\omega_2 \simeq (2\pi)11.55 \text{ GHz}$, obtaining $2g_{21} = \omega_2 - \omega_1 \simeq (2\pi)220 \text{ MHz}$ close to the full hybridization, and thus with $\alpha \simeq 0.5$.

The cavity is equipped with a hole on one side, hosting an approximately 1-cm diameter loop to generate a known test field b_1 parallel to the static field B_0 . A scope measures the current provided to the loop to infer the generated field. The current-to-field conversion constant is measured by analyzing the effect of the loop dc field on the Larmor frequency of the YIG sample, accessible by working in the dispersive regime. The conversion constant is $4.8 \mu\text{T/A}$, and is compatible with the calculated loop field. Two more measurements followed, which are performed using a sensing coil with a diameter of about 1 mm, much smaller than the loop. In the first one, an approximate 100-Hz frequency field amplitude is compared with one at high frequency. We find a 10% decrease in the field amplitude due to the operation at 220 MHz, which is probably related to the loop impedance. The second one is performed to take into account the screening effect of the cavity walls. We use the sensing coil to measure the loop field at the position of the YIG sphere with and without the cavity. The ratio of the two gives a reduction factor of

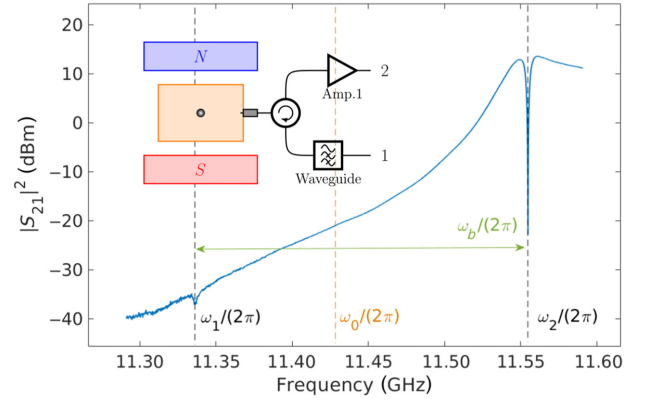


FIG. 3. The S_{21} spectrum of the system presented in the inset. The two absorption profiles are at the frequencies of the two hybrid modes ω_1 and ω_2 . The waveguide cutoff is roughly at the frequency ω_0 . The setup in the inset has the same color legend as described in Fig. 2.

$k_b = 0.09 \pm 0.03$. The overall current-to-field conversion is $4.8 \mu\text{T/A} \times 0.9 \times k_b = (0.39 \pm 0.11)\mu\text{T/A}$. The generator for the pump A_p can deliver a power up to 26 dBm, injected to an in-house fabricated waveguide with a cut-off frequency at about ω_0 . The waveguide has a cross section of $12.8 \times 6.3 \text{ mm}^2$. The antenna is movable in order to choose appropriate coupling. The two amplifiers are low noise high-electron-mobility transistors (HEMTs), with nominal gains $G_1 = 34 \text{ dB}$, $G_2 = 35 \text{ dB}$, and the bandpass filter is composed of a resonant cavity tuned to ω_2 . The readout is performed with a spectrum analyzer.

Figure 3 shows a spectroscopic measurement of the PMHS, from which we measure $\gamma_1 \simeq (2\pi)2.2 \text{ MHz}$, $\gamma_2 \simeq (2\pi)4.2 \text{ MHz}$. Magnonic dissipation limits the coherence of this PMHS, as the magnon linewidth is estimated to be of about 3.6 MHz. The asymmetry of the modes is adjusted to match the waveguide transmission, and is not expected to have an important impact on the sensor. The antenna couplings to the hybrid modes are $\beta_1 \simeq 0.3$ at ω_1 , and $\beta_2 \simeq 1$ at ω_2 . Even with the bandpass filter, these couplings are necessary to avoid the saturation of the amplifier due to the pump, and still extract some power from ω_1 . The reflected tone power at ω_2 is reduced by more than 30 dB. By injecting calibrated rf signals into the antenna input of the circulator (see Fig. 2), we measure $T_s \simeq 337 \text{ K}$, compatible with the amplifiers specifications. We feed the system with a pump of power $A_p^2 = 0.2 \text{ mW}$ at the antenna input. Following Eq. (7), the expected sensitivity is

$$\sigma_{b_1} = 1.9 \text{ pT}/\sqrt{\text{Hz}}. \quad (8)$$

We recall that this spin magnetometer is sensitive to a field at frequency $2g_{21} \simeq (2\pi)220 \text{ MHz}$ on a bandwidth as large as the linewidth γ_1 .

The system is tested using the small loop placed on the cavity side hole (see Fig. 2). Figure 4(a) shows the

spectra of the output signal for different input test fields. The experimental points reported in Fig. 4(b) show the voltage A_s measured on a $R = 50 \Omega$ load at the signal frequency $\omega_1 \simeq (2\pi)11.33$ GHz versus the field generated with the loop. The errors on the values A_s are estimated from repeated measurements with the same input field; they account for approximately 18% of the average value and are essentially due to instabilities in the experimental setup. The uncertainty on the input field, 28%, is almost totally due to the determination of the loop current-to-field coefficient. Data are fitted with a linear function, giving the slope $m_{\text{fit}} = (1.1 \pm 0.3) \times 10^5$ V/T. The expected value, derived from Eq. (5), is

$$\begin{aligned} \frac{\sqrt{RP_s(\omega_1)}}{b_1} &= \sqrt{RG_1G_2c_1} \frac{\pi\alpha Q_2^L A_p}{2\eta B_0} \\ &= (1.6 \pm 0.3) \times 10^5 \text{ V/T}, \end{aligned} \quad (9)$$

where the total gain $G_1G_2c_1 = 56 \pm 1$ dB is measured independently. The discrepancy can be due to unaccounted losses in the cables, but essentially the measured value agrees with the expected one, confirming the validity of the proposed device.

From this data we obtain the noise $P_n = -99.8$ dBm with a resolution bandwidth of $\text{RBW} = 100$ Hz, resulting in a voltage sensitivity of 2.2×10^{-7} V/ $\sqrt{\text{Hz}}$. By using the measured transduction coefficient m_{fit} , the field sensitivity is

$$\sigma_{b_1}^s = (2.0 \pm 0.7) \text{ pT}/\sqrt{\text{Hz}}, \quad (10)$$

which agrees with the calculated one given in Eq. (8). The noise level at the cavity output results $P_n^i = P_n/(G_1G_2c_1) = (2.6 \pm 0.5) \times 10^{-21}$ W/Hz. In the absence of waveguide filtering, the pump noise at ω_1 would be approximately 10^{-19} W/Hz, orders of magnitude higher than the measured thermal noise. By removing the waveguide we verified that the noise grows, and test signals have to be increased to obtain the same SNR. We conclude that the pump noise has been drastically reduced in this setup, and that the limiting background of the apparatus is mostly due to room-temperature thermodynamic fluctuations. The negative offset's origin is unclear, but it might be attributed to systematic uncertainties in the measurement.

The time response of the system is limited by the relaxation time of the hybrid modes and is of order 100 ns. The maximum measurable field is given by the condition $Q_1b_1 \ll B_0$, which holds up to tens of microtesla amplitudes. The operational bandwidth is an interval of width γ_1 centered at ω_1 . The CMP frequencies are tuned by varying the static field B_0 , allowing us to obtain an effective bandwidth of hundreds of megahertz [49]. The loop on the cavity side, which has been used for testing the setup, can be coupled to an external pick-up coil. With such a scheme,

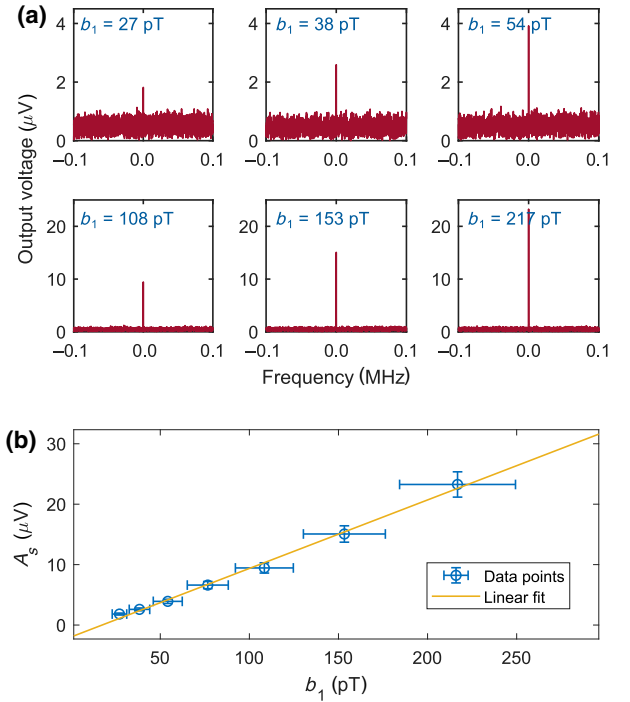


FIG. 4. (a) Signal spectra obtained with different test loop fields. The x axis is the frequency offset from $\omega_1/2\pi$, while the y axis is the voltage read at the spectrum analyser. The top-left spectrum corresponds to a $\text{SNR} = 1$ field with a resolution bandwidth of 100 Hz, i.e., an integration time of 10 ms. (b) Test measurement of the spin magnetometer, showing the voltage at ω_1 versus the calculated input field generated with the loop. The noise level is subtracted from the data points, which are then fitted to a linear function, giving a slope $m_{\text{fit}} = (1.1 \pm 0.3) \times 10^5$ V/T and an intercept $q_{\text{fit}} = (-1.9 \pm 0.7) \mu\text{V}$.

it will be possible to measure magnetic fields not directly located on the YIG sample. By properly designing the loop impedance, optimum matching conditions can be achieved with the pick-up loop. We also expect the factor k_b to be much closer to one in an optimized apparatus, allowing for a good transduction of an external signal to the PMHS.

IV. OUTLOOK AND CONCLUSIONS

The sensitivity can be further pushed by increasing the tone power; however, this value is limited due to either nonlinearities of the YIG or thermal-induced instabilities that may arise. By using a cryogenically cooled device coupled with an ultralow noise first-stage amplifier, the limiting noise could be reduced to the standard quantum limit. By replacing the factor $k_B T_s$ with $\hbar\omega$ in Eq. (7), the quoted value $\sigma_{b_1} \simeq 8$ fT/ $\sqrt{\text{Hz}}$ can be further reduced to $\sigma_{b_1} \simeq 0.3$ fT/ $\sqrt{\text{Hz}}$.

As the device sensitivity is not dependent on its size, one can engineer a much smaller PMHS, consisting for example in printed circuits or dielectric cavities coupled to a suitable magnetic material. Miniaturization may allow

for simpler construction and implementation of the device. Multiplexing is also a possibility, for example by means of superconducting circuits [50–52] resonating within the magnetometer bandwidth, which have demonstrated quality factors up to 10^8 [53–55]. Thanks to the present demonstration of the measurement scheme, forthcoming works will study alternative implementations of the magnetometer, and the device itself on a more detailed level, including for example the experimental demonstration of its dynamical bandwidth, the long-term stability of the setup, and an improved sensitivity.

In conclusion, we have devised and tested a spin magnetometer based on the phase modulation of cavity magnon polaritons. Our prototype demonstrates the working principle of the device by showing a picotesla field sensitivity, and an optimized version of the same setup could measure magnetic fields with $fT/\sqrt{\text{Hz}}$ precision. The tested design is not the only realization of the experimental scheme, which can be implemented in a number of different configurations. The magnetometer has a variable input impedance, a large dynamic range, and a remarkable sensitivity, allowing for its application for example in the field of magnetic imaging. All these features are unprecedented, and make this instrument a class of magnetometers based on the photon-magnon hybrid system.

ACKNOWLEDGMENTS

We acknowledge Enrico Berto, Mario Tessaro, and Fulvio Calaon for their work on the building and operation of the prototype. We thank Federico Chioffi, Caterina Braggio, Antonello Ortolan, and Pierre Sikivie for the stimulating discussion regarding the physics of the instrument. The support of INFN-Laboratori Nazionali di Legnaro and of INFN-CNTT is deeply acknowledged. The authors declare that there is a pending patent application related to this research.

-
- [1] R. C. Jaklevic, John Lambe, A. H. Silver, and J. E. Mercereau, Quantum Interference Effects in Josephson Tunneling, *Phys. Rev. Lett.* **12**, 159 (1964).
 - [2] S. N. Erné, H.-D. Hahlbohm, and H. Lübbig, Theory of rf-biased superconducting quantum interference device for nonhysteretic regime, *J. Appl. Phys.* **47**, 5440 (1976).
 - [3] Marco Aprili, The nanosquid makes its debut, *Nat. Nanotechnol.* **1**, 15 (2006).
 - [4] R. Kleiner, D. Koelle, F. Ludwig, and J. Clarke, Superconducting quantum interference devices: State of the art and applications, *Proc. IEEE* **92**, 1534 (2004).
 - [5] Clarke John and Alex I. Braginski, *The SQUID Handbook* (John Wiley & Sons, Weinheim, 2005).
 - [6] I. K. Kominis, T. W. Kornack, J. C. Allred, and M. V. Romalis, A subfemtotesla multichannel atomic magnetometer, *Nature* **422**, 596 (2003).
 - [7] I. M. Savukov, S. J. Seltzer, M. V. Romalis, and K. L. Sauer, Tunable Atomic Magnetometer for Detection of Radio-Frequency Magnetic Fields, *Phys. Rev. Lett.* **95**, 063004 (2005).
 - [8] Dmitry Budker and Michael Romalis, Optical magnetometry, *Nat. Phys.* **3**, 227 (2007).
 - [9] Lukasz J. Zielinski, Shin Utsuzawa, Mason Greer, Yi-Qiao Song, and Martin Hürlimann, Remote Detection of Earth's Field Nuclear Magnetic Resonance with a Robust Induction Magnetometer, *Phys. Rev. Appl.* **13**, 051002 (2020).
 - [10] Ya. S. Greenberg, Application of superconducting quantum interference devices to nuclear magnetic resonance, *Rev. Mod. Phys.* **70**, 175 (1998).
 - [11] John Clarke, Michael Hatridge, and Michael Mößle, Squid-detected magnetic resonance imaging in microtesla fields, *Annu. Rev. Biomed. Eng.*, **9**, 389 (2007). PMID: 17328671
 - [12] Vadim S. Zotev, Andrei N. Matlashov, Petr L. Volegov, Algis V. Urbaitis, Michelle A. Espy, and Robert H. Kraus Jr., SQUID-based instrumentation for ultralow-field MRI, *Supercond. Sci. Technol.* **20**, S367 (2007).
 - [13] T. Fedele, H. J. Scheer, M. Burghoff, G. Curio, and R. Körber, Ultra-low-noise EEG/MEG systems enable bimodal non-invasive detection of spike-like human somatosensory evoked responses at 1 kHz, *Physiol. Meas.* **36**, 357 (2015).
 - [14] J.-H. Storm, D. Drung, M. Burghoff, and R. Körber, A modular, extendible and field-tolerant multichannel vector magnetometer based on current sensor SQUIDs, *Supercond. Sci. Technol.* **29**, 094001 (2016).
 - [15] D. Drung, C. Abmann, J. Beyer, A. Kirste, M. Peters, F. Ruede, and T. Schurig, Highly sensitive and easy-to-use squid sensors, *IEEE Trans. Appl. Supercond.* **17**, 699 (2007).
 - [16] J.-H. Storm, P. Hömmen, N. Höfner, and R. Körber, Detection of body noise with an ultra-sensitive SQUID system, *Meas. Sci. Technol.* **30**, 125103 (2019).
 - [17] I. M. Savukov and M. V. Romalis, Nmr Detection with an Atomic Magnetometer, *Phys. Rev. Lett.* **94**, 123001 (2005).
 - [18] I. M. Savukov, S. J. Seltzer, and M. V. Romalis, Detection of nmr signals with a radio-frequency atomic magnetometer, *J. Magn. Reson.* **185**, 214 (2007).
 - [19] H. Xia, A. Ben-Amar Baranga, D. Hoffman, and M. V. Romalis, Magnetoencephalography with an atomic magnetometer, *Appl. Phys. Lett.* **89**, 211104 (2006).
 - [20] W. Wasilewski, K. Jensen, H. Krauter, J. J. Renema, M. V. Balabas, and E. S. Polzik, Quantum Noise Limited and Entanglement-Assisted Magnetometry, *Phys. Rev. Lett.* **104**, 133601 (2010).
 - [21] J. C. Allred, R. N. Lyman, T. W. Kornack, and M. V. Romalis, High-Sensitivity Atomic Magnetometer Unaffected by Spin-Exchange Relaxation, *Phys. Rev. Lett.* **89**, 130801 (2002).
 - [22] Arne Wickenbrock, Huijie Zheng, Lykourgos Bougas, Nathan Leefer, Samer Afach, Andrey Jarmola, Victor M. Acosta, and Dmitry Budker, Microwave-free magnetometry with nitrogen-vacancy centers in diamond, *Appl. Phys. Lett.* **109**, 053505 (2016).
 - [23] J. M. Taylor, P. Cappellaro, L. Childress, L. Jiang, D. Budker, P. R. Hemmer, A. Yacoby, R. Walsworth, and M. D. Lukin, High-sensitivity diamond magnetometer with nanoscale resolution, *Nat. Phys.* **4**, 810 (2008).
 - [24] Juho Luomahaara, Visa Vesterinen, Leif Grönberg, and Juha Hassel, Kinetic inductance magnetometer, *Nat. Commun.* **5**, 4872 (2014).

- [25] I. Baumgart, J.-M. Cai, A. Retzker, M. B. Plenio, and Ch. Wunderlich, Ultrasensitive Magnetometer Using a Single Atom, *Phys. Rev. Lett.* **116**, 240801 (2016).
- [26] S. Forstner, S. Prams, J. Knittel, E. D. van Ooijen, J. D. Swaim, G. I. Harris, A. Szorkovszky, W. P. Bowen, and H. Rubinsztein-Dunlop, Cavity Optomechanical Magnetometer, *Phys. Rev. Lett.* **108**, 120801 (2012).
- [27] Gianni Di Domenico, Hervé Saudan, Georg Bison, Paul Knowles, and Antoine Weis, Sensitivity of double-resonance alignment magnetometers, *Phys. Rev. A* **76**, 023407 (2007).
- [28] F. Giazotto and F. Taddei, Hybrid superconducting quantum magnetometer, *Phys. Rev. B* **84**, 214502 (2011).
- [29] Derek F. Jackson Kimball, Alexander O. Sushkov, and Dmitry Budker, Precessing Ferromagnetic Needle Magnetometer, *Phys. Rev. Lett.* **116**, 190801 (2016).
- [30] Tadas Pyragius, Hans Marin Florez, and Thomas Fernholz, Voigt-effect-based three-dimensional vector magnetometer, *Phys. Rev. A* **100**, 023416 (2019).
- [31] Akihiro Kuwahata, Takahiro Kitaizumi, Kota Saichi, Takumi Sato, Ryuji Igarashi, Takeshi Ohshima, Yuta Masuyama, Takayuki Iwasaki, Mutsuko Hatano, Fedor Jelezko, Moriaki Kusakabe, Takashi Yatsui, and Masaki Sekino, Magnetometer with nitrogen-vacancy center in a bulk diamond for detecting magnetic nanoparticles in biomedical applications, *Sci. Rep.* **10**, 2483 (2020).
- [32] S. P. Wolski, D. Lachance-Quirion, Y. Tabuchi, S. Kono, A. Noguchi, K. Usami, and Y. Nakamura, Dissipation-Based Quantum Sensing of Magnons with a Superconducting Qubit, *Phys. Rev. Lett.* **125**, 117701 (2020).
- [33] N. Crescini, C. Braggio, G. Carugno, A. Ortolan, and G. Ruoso, Cavity magnon polariton based precision magnetometry, *Appl. Phys. Lett.* **117**, 144001 (2020).
- [34] Vladislav Gerginov, F. Silva, and David Howe, Prospects for magnetic field communications and location using quantum sensors, *Rev. Sci. Instrum.* **88**, 125005 (2017).
- [35] Gian Luca Romani, Samuel J. Williamson, and Lloyd Kaufman, Biomagnetic instrumentation, *Rev. Sci. Instrum.* **53**, 1815 (1982).
- [36] Karsten Sternickel and Alex I. Braginski, Biomagnetism using SQUIDS: Status and perspectives, *Supercond. Sci. Technol.* **19**, S160 (2006).
- [37] N. Crescini, D. Alesini, C. Braggio, G. Carugno, D. D'Agostino, D. Di Gioacchino, P. Falferi, U. Gambardella, C. Gatti, G. Iannone, C. Ligi, A. Lombardi, A. Ortolan, R. Pengo, G. Ruoso, and L. Taffarello, Axion Search with a Quantum-Limited Ferromagnetic Haloscope, *Phys. Rev. Lett.* **124**, 171801 (2020).
- [38] N. Crescini, D. Alesini, C. Braggio, G. Carugno, D. Di Gioacchino, C. S. Gallo, U. Gambardella, C. Gatti, G. Iannone, G. Lamanna, C. Ligi, A. Lombardi, A. Ortolan, S. Pagano, R. Pengo, G. Ruoso, C. C. Speake, and L. Taffarello, Operation of a ferromagnetic axion haloscope at $m_a = 58 \mu\text{eV}$, *Eur. Phys. J. C* **78**, 703 (2018).
- [39] Dany Lachance-Quirion, Yutaka Tabuchi, Arnaud Glippe, Koji Usami, and Yasunobu Nakamura, Hybrid quantum systems based on magnonics, *Appl. Phys. Express* **12**, 070101 (2019).
- [40] Hans Huebl, Christoph W. Zollitsch, Johannes Lotze, Fredrik Hocke, Moritz Greifenstein, Achim Marx, Rudolf Gross, and Sebastian T. B. Goennenwein, High Cooperativity in Coupled Microwave Resonator Ferrimagnetic Insulator Hybrids, *Phys. Rev. Lett.* **111**, 127003 (2013).
- [41] A. A. Clerk, K. W. Lehnert, P. Bertet, J. R. Petta, and Y. Nakamura, Hybrid quantum systems with circuit quantum electrodynamics, *Nat. Phys.* **16**, 257 (2020).
- [42] V. Cherepanov, I. Kolokolov, and V. L'vov, The saga of yig: Spectra, thermodynamics, interaction and relaxation of magnons in a complex magnet, *Phys. Rep.* **229**, 81 (1993).
- [43] E. G. Spencer, R. C. LeCraw, and A. M. Clogston, Low-Temperature Line-Width Maximum in Yttrium Iron Garnet, *Phys. Rev. Lett.* **3**, 32 (1959).
- [44] R. C. LeCraw, E. G. Spencer, and C. S. Porter, Ferromagnetic resonance line width in yttrium iron garnet single crystals, *Phys. Rev.* **110**, 1311 (1958).
- [45] Charles Kittel, *Introduction to Solid State Physics* (Wiley, New York, 2004), 8th ed.
- [46] Lev D. Landau and Evgenij M. Lifshitz, *Theoretical Physics IX - Statistical Physics II: Theory of the Condensed State* (Editori riuniti - University Press, 2010).
- [47] Daniel F. Walls and Gerard J. Milburn, *Quantum Optics* (Springer Science & Business Media, New York, 2007).
- [48] T. M. Fortier, C. W. Nelson, A. Hati, F. Quinlan, J. Taylor, H. Jiang, C. W. Chou, T. Rosenband, N. Lemke, A. Ludlow, D. Howe, C. W. Oates, and S. A. Diddams, Sub-femtosecond absolute timing jitter with a 10 ghz hybrid photonic-microwave oscillator, *Appl. Phys. Lett.* **100**, 231111 (2012).
- [49] N. Crescini, C. Braggio, G. Carugno, R. Di Vora, A. Ortolan, and G. Ruoso, Magnon-driven dynamics of a hybrid system excited with ultrafast optical pulses, *Commun. Phys.* **3**, 164 (2020).
- [50] K. D. Irwin and K. W. Lehnert, Microwave squid multiplexer, *Appl. Phys. Lett.* **85**, 2107 (2004).
- [51] J. A. B. Mates, G. C. Hilton, K. D. Irwin, L. R. Vale, and K. W. Lehnert, Demonstration of a multiplexer of dissipationless superconducting quantum interference devices, *Appl. Phys. Lett.* **92**, 023514 (2008).
- [52] Sebastian Kempf, Mathias Wegner, Andreas Fleischmann, Loredana Gastaldo, Felix Herrmann, Maximilian Papst, Daniel Richter, and Christian Enss, Demonstration of a scalable frequency-domain readout of metallic magnetic calorimeters by means of a microwave squid multiplexer, *AIP Adv.* **7**, 015007 (2017).
- [53] L. Frunzio, A. Wallraff, D. Schuster, J. Majer, and R. Schoelkopf, Fabrication and characterization of superconducting circuit qed devices for quantum computation, *IEEE Trans. Appl. Supercond.* **15**, 860 (2005).
- [54] Matthew Reagor, Wolfgang Pfaff, Christopher Axline, Reinier W. Heeres, Nissim Ofek, Katrina Sliwa, Eric Holland, Chen Wang, Jacob Blumoff, Kevin Chou, Michael J. Hatridge, Luigi Frunzio, Michel H. Devoret, Liang Jiang, and Robert J. Schoelkopf, Quantum memory with millisecond coherence in circuit qed, *Phys. Rev. B* **94**, 014506 (2016).
- [55] A. Bruno, G. de Lange, S. Asaad, K. L. van der Eenden, N. K. Langford, and L. DiCarlo, Reducing intrinsic loss in superconducting resonators by surface treatment and deep etching of silicon substrates, *Appl. Phys. Lett.* **106**, 182601 (2015).